ADVANCED FUNCTIONAL MATERIALS
www.afm-journal.de

Materials Views
www.MaterialsViews.com

Interactive Growth Effects of Rare-Earth Nanoparticles on Nanorod Formation in $YBa_2Cu_3O_x$ Thin Films

F. Javier Baca, Timothy J. Haugan, Paul N. Barnes, Terry G. Holesinger, Boris Maiorov, Rongtao Lu,* Xiang Wang, Joshua N. Reichart, and Judy Z. Wu**

The controlled growth of self-assembled second-phase nanostructures has been shown to be an essential tool for enhancing properties of several composite oxide thin film systems. Here, the role of Y_2O_3 nanoparticles on the growth of $BaZrO_3$ (BZO) nanorods is investigated in order to understand the mechanisms governing their self-assembly in $YBa_2Cu_3O_{7-x}$ (YBCO) thin films and to more fully control the resulting defect landscape. By examining the microstructure and current-carrying capacity of BZO-doped YBCO films, it is shown that the nanorod growth dynamics are significantly enhanced when compared to films double-doped with BZO and Y_2O_3 nanoparticles. The average nanorod length and associated critical current densities are found to increase at a significantly higher rate in the absence of Y_2O_3 nanoparticles when the growth temperature is increased. Using microstructural data from transmission electron microscopy studies and the response in critical current density, the interactive effects of multiple dopants that must be considered to fully control the defect landscape in oxide thin films are shown.

1. Introduction

The importance of nanostructured materials have been emphasized in several application areas, including ferroelectric and multiferroic oxides,[1,2] magnetic oxides,[3] and superconducting cuprates.[4–6] In each of these cases, the functional performance of the material may be directly refined through microstructure engineering. For superconducting $YBa_2Cu_3O_x$ (YBCO) thin films, a highly tuned defect landscape is necessary to maximize performance in magnetic fields of varied strength and orientation; inclusions of insulating phases, such as $BaZrO_3$ (BZO), $BaSnO_3$ YBa_2NbO_6, and the rare-earth tantalates, have been identified as promising routes toward achieving this.[4,6–10]

Columnar BZO nanorods that self-assemble in the YBCO matrix can provide strong vortex pinning centers, thus improving the current-carrying capacity in the presence of a magnetic field, the critical current density $J_c(H)$.[6,11–16] While growth dynamics have been shown to play a vital role in the self-assembly of the BZO nanorods, the effects of multiple dopant phases on their formation have not been explicitly identified.[17] Maiorov et al. showed that the temperature of the substrate during growth (T_g) directly influences the linearity, length, and splay of BZO nanorods in composite YBCO thin films doped with 5 mol% (2.6 vol%) Y_2O_3 and 5 mol% (2.3 vol%) $BaZrO_3$.[17] In part, the increasing affinity for nanorod growth is due to the overall increase in mobility with increased growth temperature, which allows for BZO migration and promotes the self-assembly of nanorods. However, with its significantly higher melting temperature of approximately 2410 °C, the excess Y_2O_3 is less mobile, and the smaller lattice misfit to YBCO reduces the likelihood for strain-driven self-assembly, thus remaining in the form of nanoparticle inclusions. An interaction between the multiple dopant phases (e.g., Y_2O_3 and $BaZrO_3$) during film growth should be expected, and we show that significant microstructural and vortex pinning effects result from the induced changes in the BZO nanorod self-assembly.

Dr. F. J. Baca, Dr. T. G. Holesinger, Dr. B. Maiorov
Los Alamos National Laboratory
Los Alamos, NM 87545, USA
E-mail: f.javier.baca@gmail.com
Dr. F. J. Baca, Dr. T. J. Haugan, Dr. P. N. Barnes, J. N.Reichart
U.S. Air Force Research Laboratory
Propulsion Directorate
Wright-Patterson Air Force Base, OH 45433, USA
Dr. F. J. Baca, Dr. R. Lu, Dr. X. Wang, Prof. J. Z. Wu
University of Kansas
Department of Physics and Astronomy
Lawrence, KS 66045, USA
E-mail: jwu@ku.edu; rtlu@ku.edu

DOI: 10.1002/adfm.201203660

2. Microstructural Results

Microstructural evidence of the influence of growth temperature on BZO nanorod growth is shown by cross-sectional transmission electron microscopy (TEM) in **Figure 1**. This figure shows the typical evolution of the microstructures observed for YBCO films doped with 2 vol% BZO for growth temperatures ranging from 780 to 835 °C. A general trend of increasing BZO nanorod length and continuity is observed with increasing growth temperature. From measurements made on multiple cross-sectional images over different regions of the films grown at varied substrate temperatures, the observable length of continuous nanorods increases on average from 46.3 to 118 nm for increasing T_g from 780 to 835 °C. The average nanorod

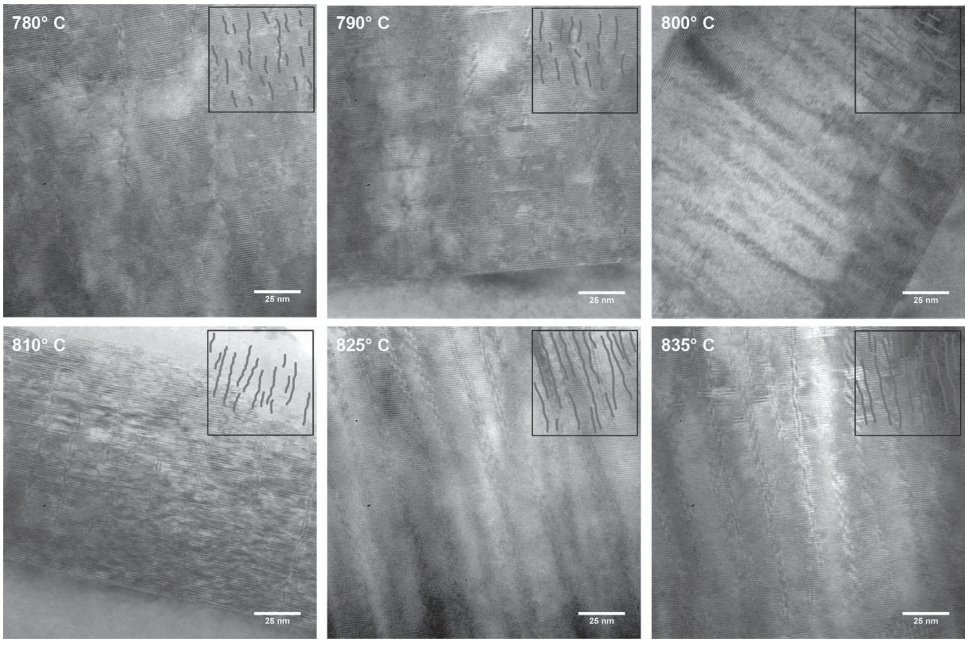

Figure 1. Cross-sectional bright-field TEM images of YBCO thin films doped with 2 vol% BZO. Images are shown for growth temperatures of 780–835 °C, and the overlaid lines in the inset illustrate the paths of the BZO nanorods through the film. The scale bars represent 25 nm.

diameters remain nearly constant, within the standard deviation of the measurements, and range from 4.7–6.0 nm. Additionally, the overall alignment of the BZO nanorods relative to the YBCO *c*-axis increases, with the average angle of deviation from $[001]_{YBCO}$ decreasing from 10.6° to 6.3° over the same range of T_g.

The increase in average length and decrease in splay is generally consistent with that observed for YBCO films doped with BZO and Y_2O_3, however, when the trends are compared quantitatively, notable changes are observed. **Figure 2** shows these trends explicitly, by plotting the average nanorod length measured in films single-doped with BZO (plotted in solid symbols) with those doped with both BZO and Y_2O_3 by Maiorov et al. (plotted with open symbols).[17] In this figure, it is seen that the average nanorod length increases quickly with growth temperature, which is likely a response to the added mobility and increased rate of Zr^+ diffusion through the matrix. Thus, the nanorods are more likely to grow into longer columns at the expense of shorter BZO nanorod segments. It is, however, apparent that over the temperature range of 780–835 °C, the measured rate of increase of average length with respect to growth temperature is considerably higher than that reported for the Y_2O_3-rich YBCO films. Since the double- and single-doped samples were grown in different experimental apparatus, the possible issue of temperature calibration and scaling will be further discussed below. Figures 1 and 2 do, however, give preliminary indication of the interaction between the rare-earth nanoparticles and BZO within the YBCO matrix, and shows an overall impeding effect of the Y_2O_3 on the nanorod self-assembly. It is noteworthy that the segregation and self-assembly of the dopant phase into nanorods is largely mediated by the thermodynamics of the multiphase system, as well as by the strain induced by the geometrically mismatched lattices. With a relatively small mismatch (ca. 1.3%) between the single-crystal $SrTiO_3$ substrate and the YBCO matrix, the interfacial strain is dominated by the mismatch between the matrix and dopant phases.[15,18] This has been demonstrated in mechanical models, which show the morphology and geometric alignment of self-assembled nanorods to be a function of the interfacial elastic strain between the YBCO matrix and substrate and that between YBCO and BZO.[19–21] The extreme case of substrate/matrix-dominated strain distributions may result in nanorods aligned perpendicular to the YBCO *c*-axis.[20] In addition, these models of strain-induced self-assembly have estimated the

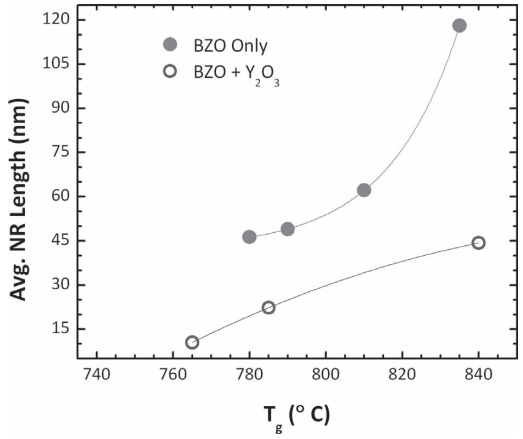

Figure 2. Average BZO nanorod length in YBCO matrix as a function of growth temperature. The filled symbols show data points for single-doped films while the open sybols are for YBCO + BZO + Y_2O_3 from Maiorov et al.[17]

interaction length to be on the order of several nanometers, which is small compared to the film thicknesses of practical application.[20,21] Therefore, the dominant effects from strained interfaces are induced by the lattice mismatch between the YBCO matrix and the dopant phases. This is in contrast to the case of self-assembled pore nanotube arrays in YBCO films we investigated previously,[22,23] in which the local interfacial strain initiates pore formation via nanoparticle precipitation or addition[24,25] and manages to extend to large distance—up to micrometers—if high-quality crystallinity of the matrix film can be maintained at large thickness.[23,26] In the case of BZO-doped YBCO, the interfacial strain effect may be significantly enhanced at higher T_g as the crystallinity of both the YBCO and dopants are improved and, consequently, the coherency of their interfaces is increased.[27,28] The enhanced strain and dopant mobility at elevated growth temperature together may explain the concave-upward nanorod length vs. T_g curve in Figure 2 in the absence of Y_2O_3 particles. It is also worth noting that the negative lattice misfit between Y_2O_3 and YBCO causes a compressive strain on the matrix, as opposed to the tensile strain induced by the BZO additions. Therefore, the presence of Y_2O_3 particles could locally reduce the net strain on the YBCO lattice due to the BZO, thus potentially affecting the self-assembly of nanorods and resulting in a qualitatively different temperature dependence of the nanorod length.

3. Vortex Pinning Effects

The change in vortex pinning with increasing growth temperature is significant, as is evident in **Figure 3** where the magnetic critical current density is shown as a function of applied magnetic field for $H \parallel c$, measured at 77 and 65 K. Overall, at both temperatures, an increasing trend in $J_c(H)$ is observed with increasing T_g. At 77 K, the largest increases occur as the growth temperature is raised from the lowest value of 780 °C, but $J_c(H)$ continues to consistently increase until $T_g \approx 825$ °C. An enhancement in $J_c(H \parallel c)$ is expected, given the high vortex pinning force density provided by the longer lengths of non-superconducting BZO along the film thickness. However, an interesting feature is observed at the lowest T_g, where $J_c(H \parallel c)$ is less than that of the undoped YBCO film for magnetic fields above approximately 0.2 T at 77 K. Although columnar pinning sites are available even at the lowest T_g, the average length of the nanorods is approximately 46 nm. These short segments of columnar defects may fall below the threshold for correlated vortex pinning, as predicted by Rodriguez et al.[29,30] However, the available volume of superconducting material is still accordingly reduced by the insulating inclusions. Thus, an overall reduction of the critical current density results from the current-blocking effect of the BZO or by causes that are not yet fully understood in doped YBCO films.[29–31] Examining $J_c(H, 65\ K)$, we see in Figure 3 that for the lowest T_g, the crossover in $J_c(H)$ increases by nearly a factor of 10 to $H = 2.3$ T. This large increase is likely due to the relatively large splay of the nanorods at low T_g and the reduced vortex creep at the lower temperature.[32] Additionally, the interfacial region surrounding BZO nanorods has been shown to produce an effective sheath of oxygen-deficient YBCO that results in reduced T_c.[33] The band of lower-T_c material would produce a larger defect diameter at higher temperatures, thus reducing $J_c(H)$ at lower fields.

A consistent trend is observed in **Figure 4**, which shows the transport J_c as a function of the incidence angle of the magnetic field, θ, for 1 and 3 T, measured at 77 K. An increase of approximately 48% is seen in $J_c(H \parallel c)$ when T_g is increased from 810 to 825 °C at 1 T. Comparably, an increase of roughly 45% is shown for the same conditions at 3 T. This is consistent with the pinning effects shown in Figure 3, and it is worth noting that the peak at $H \parallel c$ ($\theta = 0°$) is only slightly broadened at the lower T_g. While the overall increase in $J_c(H \parallel c)$ is again attributable to the increased average length of the nanorods with higher T_g (as shown in Figure 2), the small difference in the peak width reflects the small decrease of roughly 1.1° in the average nanorod splay. The comparable change in $J_c(H \parallel c)$ for both 1 and 3 T reflects the matching field of the nanorod number density being near or above 3 T, as shown below by examination of the net pinning force.

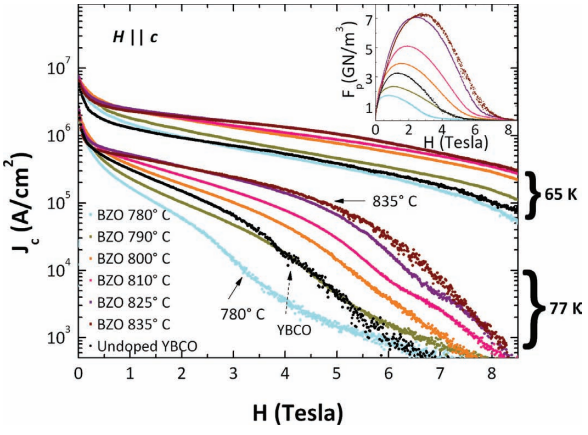

Figure 3. J_c vs. applied magnetic field measured at 77 and 65 K with $H \parallel c$ for YBCO films with 2 vol% BZO with varied growth temperature. Data for an undoped sample is included as a reference. The inset shows the flux pinning force for the same set of J_c curves.

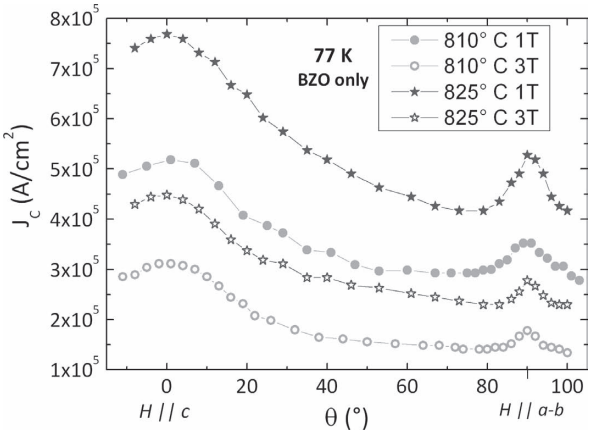

Figure 4. Transport critical current density as a function magnetic field incidence angle measured at 77 K for 1 T (filled symbols) and 3 T (open symbols) fields. The points plotted with circles show $J_c(\theta)$ for $T_g = 810$ °C and those plotted with stars are for $T_g = 825$ °C.

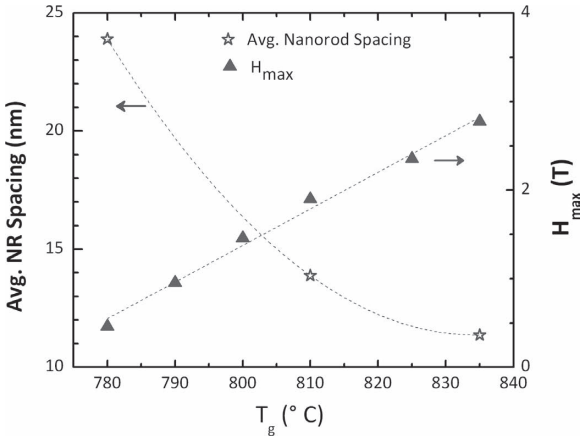

Figure 5. The left-hand axis (open symbols) shows the average separation between BZO nanorods as a function of growth temperature. The right-hand axis (filled symbols) shows values of the applied magnetic field at which the maximum flux pinning force density occurs.

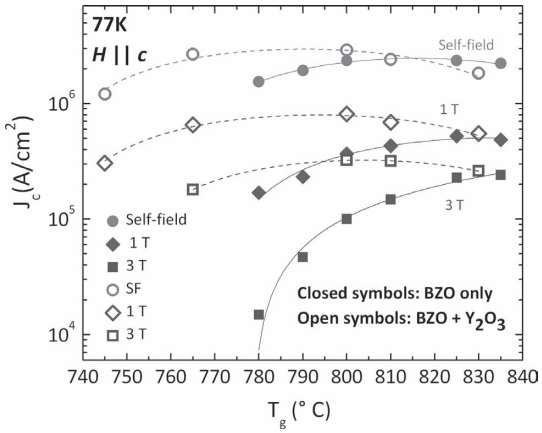

Figure 6. Critical current densities at self-field, and at 1 and 3 T as a function of growth temperature. The closed symbols are the data points for the BZO-doped films. The open symbols show the values for YBCO + BZO + Y_2O_3.[17]

The net vortex pinning force density, F_p, is shown as a function of applied magnetic field in the inset of Figure 3. It is interesting to note that both the magnitude of the maximum F_p, as well as the value, H_{max}, at which this occurs, increase with increasing T_g. The monotonic increase is clearly seen in **Figure 5** (right-hand side vertical axis), where H_{max} is plotted as a function of growth temperature. Since accommodating higher magnetic field intensities generally requires increasing the number of available vortex pinning sites, the nearly linear increase in H_{max} implies that the matching field of the defect density is increasing with T_g. This is consistent with the microstructure observed in Figure 1, where, on average, the spacing between nanorods decreases with increasing T_g. This is also shown in Figure 5 (left-hand side vertical axis), where the separation between nanorods, as averaged over 60–70 measurements per sample in multiple cross-sectional images, is seen to decrease from approximately 24 to 11 nm over the 55 °C range of T_g. Assuming a triangular lattice distribution of nanorods (where the separations measured from the cross-sectional images approximate the lattice constant), this results in an increased defect density from ca. 5.1×10^{10} to ca. 2.2×10^{11} cm^{-2}, which nearly accounts for the approximately factor of six increase in matching field. These results appear to suggest an inconsistency, since increasing both the number of nanorods and their length would imply an increase in the total BZO volume. However, the apparent additional volume of BZO may be accounted for by the reduced number density of nanoparticles, and possibly by the reduction of additional phases such as $BaZr_{2-x}Y_xO_6$ that may be less likely to form at the higher growth temperatures.

The continued increase in H_{max} and J_c ($H\iota c$) with increasing T_g further reveals the influence of Y_2O_3 particles on the nanorod growth and the vortex pinning. When YBCO is doped with both BZO and Y_2O_3, a significant turning point in the vortex pinning was observed, showing a clear decrease in $J_c(H)$ for T_g > 800 °C.[17] The persisting increase in $J_c(H)$ for the single-doped YBCO + BZO reflects the trend observed in Figures 2 and 3 of increasing nanorod length and *c*-axis alignment, and indicates the increased rate of BZO *c*-axis growth and alignment in the absence of additional Y_2O_3 particles. The effect of this turning point is clearly seen in **Figure 6**, which shows the J_c dependence on growth temperature for applied fields of 0 (self-field), 1, and 3 T at 77 K for both BZO-doped and BZO + Y_2O_3 -doped YBCO films. In this figure, the overall shape of the J_c (T_g) dependence is nearly the same for the single-dopant films as that reported by Maiorov et al. for BZO + Y_2O_3 at self-field. This similarity in the J_c (T_g) behavior is not unexpected because at self-field, where the vortex density is minimal, the pinning structure is largely irrelevant to the critical current density. However, with increasing magnetic field, more significant effects are observed. For example, at 3 T a fairly sharp increase in J_c is shown with increasing T_g for the single-doped YBCO, while a local maximum is observed for those doped with BZO + Y_2O_3. Thus, the vortex pinning behavior up to 3 T appears to support the notion that indeed the defect structures are evolving at different rates in the presence of rare-earth nanoparticles.

To emphasize the effect of the physical geometry of the defect landscape, and reduce the influence of experimental scaling and temperature calibration, **Figure 7** shows the J_c dependence on the measured nanorod length for both BZO-doped and BZO + Y_2O_3 -doped YBCO thin films. Thus, if the vortex pinning mechanisms are comparable, we would expect to find the maximum critical current density occurring for comparable defect structures. However, Figure 7 shows both a shift in the in peak position (maximum J_c for a given applied magnetic field), and that the difference in peak position is increasing with increased magnetic field *H*. Maiorov et al. suggested that the turning point in J_c (T_g) is in part caused by the reduced splay in the columnar defects leading to vortex hopping.[17] Thus, the shift in the maximum J_c for longer nanorods implies a higher level of splay is maintained for longer columnar defects in the absence of Y_2O_3 nanoparticles. An increased splay may be expected for the single-doped YBCO films, since the negative lattice mismatch between Y_2O_3 and the matrix may locally reduce the strain state and allow for more linear growth of BZO nanorods. A broadening of the $J_c(L)$ dependence for the single-doped YBCO films is also notable in Figure 7, when compared to that doped with

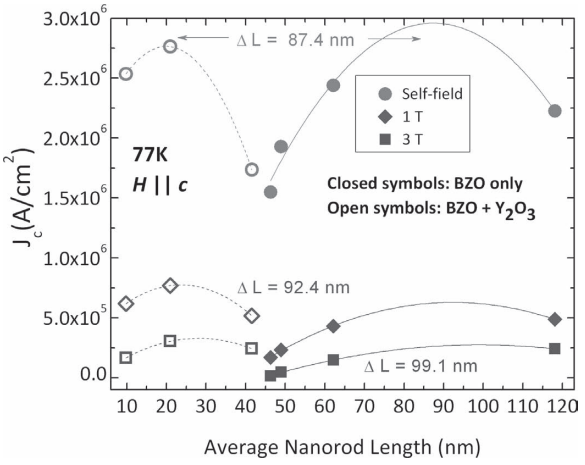

Figure 7. Critical current density at self-field, and at 1 and 3 T as a function of average BZO nanorod length. The closed symbols are the data points for the BZO-doped films. The open symbols show the values for YBCO + BZO + Y_2O_3.[17] The difference in peak positions of the fitted curves is also indicated for each magnetic field.

BZO + Y_2O_3. Thus, an increased J_c is maintained for a broader range of nanorod lengths in the absence of the rare-earth particles. The shift in the maximum J_c to longer nanorod lengths and broadening of the $J_c(L)$ dependence do, however, show that the performance and vortex pinning properties behave differently as a function of the physical geometry, independent of temperature calibration or experimental differences.

4. Dynamic Effects During Film Growth

The kinetics of thin film growth are strongly dictated by the thermal energy supplied, and the surface and bulk mobilities depend strongly on T_g. An example that illustrates this behavior is the simple case of binary diffusion. In such a system, the flux of species is described by Fick's Law, where the diffusivity depends exponentially on the growth temperature,

$$D = D_o e^{-E_d/k_B T_g} \quad (1)$$

Where E_d is an activation energy determining the barrier height that restricts the motion of the species at the growth surface, and the coefficient D_o depends on sample geometry and rate of arrival, but is independent of temperature.[34] By analogy, we may then expect increasing diffusivity with increased T_g for the YBCO/BZO system. This would then allow for an increased range of Zr^+ surface migration, and allow for continued BZO growth at sites where nucleation previously occurred. Thus, the higher T_g provides conditions favorable to longer length columnar growth rather than discrete nanoparticles or truncated nanorods. However, in the presence of multiple phases, as in the case of BZO + Y_2O_3 -doped YBCO, the diffusion of Zr^+ through the matrix is impeded by potential barriers of both the Y_2O_3 and the YBCO. Therefore, the BZO nanorod growth may be interrupted by Y_2O_3 particles, as observed by Maiorov et al.,[17] and the rate of growth slowed when compared to single-doped YBCO, as shown in Figure 2.

The self-assembly of secondary phases in composite thin films has been analyzed in terms of static interfacial interactions and, qualitatively, with respect to growth kinetics for multiple oxide systems.[3,18,28] In addition, quantitative descriptions of the self-alignment of semiconducting quantum dots have shown that strain-mediated nucleation and growth can determine the resulting geometry of the binary-phase composites.[35,36] Specifically, for the case of InAs-doped GaAs thin films, Xie et al. developed an expression for the effective probability of In adatom migration to the strain-relaxed region immediately above the preceding island.[35] With respect to the growth kinetics, this model produces a sharp maximum in the probability for geometrically correlated growth for a given growth temperature corresponding to the activation energy barrier E_d, when Equation 1 is used for the diffusivity term.[35] An analogous maximum probability for self-assembly as a function of T_g may also be expected for the YBCO + BZO system since increasing thermal energy eventually allows the Zr^+ to surpass the activation energy barrier, and the ion mobility is maximized. By this analogy, the likelihood of correlated self-assembly would increase quickly as the temperature corresponding to the activation energy is approached. The results shown in Figure 2 are consistent with this type of behavior, and indicate that the range of $T_g$considered in this experiment is still below the maximum mobility, since the roughly 7% increase in T_g over the span from 780 to 835 °C results in approximately a factor of 1.5 times increase in average nanorod length. However, when compared to the double-doped YBCO + BZO + Y_2O_3, we see in Figure 2 that the rate of increase of average nanorod length is significantly reduced as the higher range of T_g is approached. This indicates that by the analogy above, the T_g of 840 °C nearly maximizes probability for self-assembly for the double-inclusion system of both BZO and Y_2O_3 additions, and that the rate of BZO migration through the matrix is significantly slowed in the presence of Y_2O_3.

5. Conclusions

The ability to tailor the microstructure of thin films to application-specific requirements at the growth stage is desirable for several oxide systems. We have shown that in composite YBCO films, the interaction between rare-earth nanoparticles and BZO dopants produces a significant change in the growth dynamics of nanorod inclusions. In the absence of Y_2O_3 nanoparticles, the average length of BZO nanorods is significantly more sensitive to increasing growth temperature than in double-doped compositions. This results in longer columnar inclusions over comparable ranges of growth temperature, indicating the Y_2O_3 inclusions, on average, impede BZO self-assembly. The vortex pinning effects reflect this modified microstructure, showing increased J_c ($H \parallel c$) dependence and a monotonically increasing $F_{p\ max}(H)$ with increasing T_g. While the segregated growth of secondary phases in YBCO films is largely strain-mediated, adequate mobility is also necessary to allow for species migration through the matrix. The observed microstructure and increased rate of growth show that the net diffusivity may be reduced in the presence of multiple phase additions. Further experiments with varied combinations of oxide additions are planned, thus

enabling quantification of the dopant interaction and the effect on net diffusivity.

6. Experimental Section

Thin films of epitaxially grown YBCO were deposited on single-crystal $SrTiO_3$ substrates by pulsed laser deposition (PLD) using a single target with 2 vol% $BaZrO_3$. To examine the role of mobility in BZO nanorod formation, the substrate temperature was varied from 780 to 835 °C, while the other growth conditions were held constant. The fixed parameters of 300 mTorr O_2 partial pressure, 3.2 J cm^{-2} laser energy density, and an 8 Hz pulse rate were used for each deposition. A deposition rate of 33–38 nm min^{-1} for 10.25 min produced films 340–390 nm thick. The vortex pinning behavior as indicated by the $J_c(H)$ dependence as well as T_c were determined magnetically using a vibrating sample magnetometer. The resulting microstructures were characterized by cross-sectional TEM and XRD. TEM cross-sections were prepared by focused ion beam (FIB) (cut along <100> or <010>), producing 150–250 nm thick foils. Final polishing was carried out using 600–900 eV Ar ions incident at 10°–12°.

Acknowledgements

The authors acknowledge support from the Air Force Office of Scientific Research, and the Department of Energy Office of Electricity. J.Z.W. acknowledges support from NSF contracts NSF-DMR-0803149, -1105986, and NSF EPSCoR-0903806, and matching support from the State of Kansas through the Kansas Technology Enterprise Corporation.

Received: December 11, 2012
Revised: February 23, 2013
Published online: April 19, 2013

[1] H. Zheng, F. Straub, Q. Zhan, P.-L. Yang, W.-K. Hsieh, F. Zavaliche, Y.-H. Chu, U. Dahmen, R. Ramesh, *Adv. Mater.* **2006**, *18*, 2747.
[2] J. L. MacManus-Driscoll, P. Zerrer, H. Wang, H. Yang, J. Yoon, A. Fouchet, R. Yu, M. G. Blamire, Q. Jia, *Nat. Mater.* **2008**, *7*, 314.
[3] O. I. Lebedev, J. Verbeeck, G. Van Tendeloo, O. Shapoval, A. Belenchuk, V. Moshnyaga, B. Damashcke, K. Samwer, *Phys. Rev. B* **2002**, *66*, 104421.
[4] J. L. MacManus-Driscoll, S. R. Foltyn, Q. X. Jia, H. Wang, A. Serquis, L. Civale, B. Maiorov, M. E. Hawley, M. P. Maley, D. E. Peterson, *Nat. Mater.* **2004**, *3*, 439.
[5] T. J. Haugan, P. N. Barnes, R. Wheeler, F. Meisenkothen, M. Sumption, *Nature* **2004**, *430*, 867.
[6] A. Goyal, S. Kang, K. J. Leonard, P. M. Martin, A. A. Gapud, M. Varela, M. Paranthaman, A. O. Ijaduola, E. D. Specht, J. R. Thompson, D. K. Christen, S. J. Pennycook, F. A. List, *Supercond. Sci. Technol.* **2005**, *18*, 1533.
[7] C. V. Varanasi, J. Burke, J. L. Brunke, H. Wang, M. Sumption, P. N. Barnes, *J. Appl. Phys.* **2007**, *102*, 063909.
[8] D. M. Feldmann, T. G. Holesinger, B. Maiorov, S. R. Foltyn, J. Y. Coulter, I. Apodaca, *Supercond. Sci. Technol.* **2010**, *23*, 095004.
[9] S. H. Wee, A. Goyal, Y. L. Zuev, C. Cantoni, V. Selvamanickam, E. D. Specht, *Appl. Phys. Express* **2010**, *3*, 023101.
[10] S. A. Harrington, J. H. Durrell, B. Maiorov, H. Wang, S. C. Wimbush, A. Kursumovic, J. H. Lee, J. L. MacManus-Driscoll, *Supercond. Sci. Technol.* **2009**, *22*, 022001.
[11] S. Kang, A. Goyal, J. Li, A. A. Gapud, P. M. Martin, L. Heatherly, J. R. Thompson, D. K. Christen, F. A. List, M. Paranthaman, D. F. Lee, *Science* **2006**, *311*, 1911.
[12] S. R. Foltyn, L. Civale, J. L. MacManus-Driscoll, Q. X. Jia, B. Maiorov, H. Wang, M. Maley, *Nat. Mater.* **2007**, *6*, 631.
[13] K. Matsumoto, P. Mele, *Supercond. Sci. Technol.* **2010**, *23*, 014001.
[14] T. J. Haugan, F. J. Baca, M. J. Mullins, N. A. Pierce, T. A. Campbell, E. L. Brewster, P. N. Barnes, H. Wang, M. D. Sumption, *IEEE Trans. Appl. Supercond.* **2009**, *19*, 3270.
[15] F. J. Baca, P. N. Barnes, R. L. S. Emergo, T. J. Haugan, J. N. Reichart, J. Z. Wu, *Appl. Phys. Lett.* **2009**, *94*, 102512.
[16] D. M. Feldmann, T. G. Holesinger, B. Maiorov, H. Zhou, S. R. Foltyn, J. Y. Coulter, I. Apodaca, *Supercond. Sci. Technol.* **2010**, *23*, 115016.
[17] B. Maiorov, S. A. Baily, H. Zhou, O. Ugurlu, J. A. Kennison, P. C. Dowden, T. G. Holesinger, S. R. Foltyn, L. Civale, *Nat. Mater.* **2009**, *8*, 398.
[18] F. J. Baca, *PhD Thesis*, University of Kansas, Lawrence, KS, USA **2009**.
[19] J. J. Shi, J. Z. Wu, *Philos. Mag.* **2012**, *91*, 2911.
[20] J. J. Shi, J. Z. Wu, *Philos. Mag.* **2012**, *92*, 4205.
[21] S. H. Wee, Y. Gao, Y. L. Zuev, K. L. More, J. Meng, J. Zhong, G. M. Stocks, A. Goyal, *Adv. Funct.. Mater.* **2012**, doi: 10.1002/adfm.201202101.
[22] R. L. S. Emergo, J. Z. Wu, D. K. Christen, T. Aytug, *Appl. Phys. Lett.* **2004**, *85*, 70.
[23] J. Z. Wu, R. Emergo, X. Wang, G. W. Xu, T. Haugan, P. Barnes, *Appl. Phys. Lett.* **2008**, *93*, 062506.
[24] R. Emergo, J. Z. Wu, T. Haugan, P. Barnes, *Appl. Phys. Lett.* **2005**, *87*, 232503.
[25] J. Baca, D. Fisher, J. Z. Wu, *Supercon. Sci. Tech.* **2007**, *20*, 554.
[26] X. Wang, A. Dibos, J.Z. Wu, *Phys. Rev. B* **2008**, *77*, 144525.
[27] Y. F. Gao, J. Y. Meng, A. Goyal, G. M. Stocks, *J. Met.* **2008**, *9*, 54.
[28] J. L. MacManus-Driscoll, *Adv. Funct. Mater.* **2010**, *20*, 2035.
[29] J. P. Rodriguez, *Applied Superconductivity Conference*, Washington, DC, **2010**, presentation 2MY-01.
[30] J. P. Rodriguez, P. N. Barnes, C. P. Varanasi, *Phys. Rev. B* **2008**, *78*, 052505.
[31] S. C. Wimbush, M. Li, M. E. Vickers, B. Maiorov, D. M. Feldmann, Q. Jia, J. L. MacManus-Driscoll, *Adv. Funct. Mater.* **2009**, *19*, 835.
[32] L. Civale, *Supercond. Sci. Technol.* **1997**, *10*, A11.
[33] C. Cantoni, Y. Gao, S.-H. Wee, E. D. Specht, J. Gazquez, J. Meng, S. J. Pennycook, A. Goyal, *ACS Nano* **2011**, *5*, 4783.
[34] J. A. Venables, *Phys. Rev. B* **1987**, *36*, 4153.
[35] Q. Xie, A. Madhukar, P. Chen, N. P. Kobayashi, *Phys. Rev. Lett.* **1995**, *75*, 2542.
[36] J. Tersoff, C. Teichert, M. G. Lagally, *Phys. Rev. Lett.* **1996**, *76*, 1675.